

INTEGRAL study of MAXI J1535–571, MAXI J1820+070 and MAXI J1348–630 outbursts

I. Detection and polarization properties of the high-energy emission

F. Cangemi^{1,2}, J. Rodriguez³, T. Belloni⁴, C. Gouiffès³, V. Grinberg⁵, P. Laurent³, P.-O. Petrucci⁶, and J. Wilms⁷

¹ Sorbonne Université, CNRS/IN2P3, Laboratoire de Physique Nucléaire et de Hautes Energies, LPNHE, 4 place Jussieu, 75005 Paris, France

e-mail: cangemi@apc.in2p3.fr

² Université Paris-Cité, AstroParticules et Cosmologie, APC, 10 rue Alice Domon et Léonie Duquet, 75013 Paris, France

³ Université Paris-Saclay, Université Paris-Cité, CEA, CNRS, AIM, 91191, Gif-sur-Yvette, France

⁴ INAF-Osservatorio Astronomico di Brera, via E. Bianchi 46, I-23807, Merate, Italy

⁵ European Space Agency (ESA), European Space Research and Technology Centre (ESTEC), Keplerlaan 1, 2201 AZ Noordwijk, the Netherlands

⁶ Institut de Planétologie et d’Astrophysique de Grenoble, Université de Grenoble Alpes, 38000 Grenoble, France

⁷ Dr. Karl Remeis-Sternwarte and Erlangen Centre for Astroparticle Physics, Friedrich-Alexander Universität Erlangen-Nürnberg, Sternwartstr. 7, 96049 Bamberg, Germany

Accepted;

ABSTRACT

Context. In black hole X-ray binaries, a non-thermal high-energy component is sometimes detected at energies above 200 keV. The origin of this high-energy component is debated and distinct spectral modelizations can lead to different interpretations. High-energy polarimetry measurements with *INTEGRAL* allow new diagnostics on the physics responsible for the MeV spectral component in black hole X-ray binaries.

Aims. In this work, we aim to investigate the high-energy behavior of three bright sources discovered by the Monitor of All-sky X-ray Image: MAXI J1535–571, MAXI J1820+070 and MAXI J1348–630. We take advantage of their brightness to investigate their soft γ -ray (0.1–2 MeV) properties with *INTEGRAL*. We use both spectral and polarimetric approaches to probe their high-energy emission with the aim to bring new constraints on the \sim MeV emission in black hole X-ray binaries.

Methods. We first study the spectral characteristics of the sources in the 3–2000 keV using JEM-X, IBIS and SPI with a semi-phenomenological description of the data. We then use IBIS as a Compton telescope in order to evaluate the polarization properties of the sources above 300 keV.

Results. A high-energy component is detected during the Hard-Intermediate State and Soft-Intermediate State of MAXI J1535–571, the Low-Hard State of MAXI J1820+070 and the Low-Hard State of MAXI J1348–630. The components detected in MAXI J1820+070 and MAXI J1348–630 are polarized with a polarization fraction of $26 \pm 9^\circ$ and $> 56\%$ in the 300–1000 keV, respectively. With no polarization information for MAXI J1535–571, the component detected could either come from the jets rather than the corona. In the case of MAXI J1820+070, the extrapolation of the synchrotron spectrum measured in the infrared indicates that the component is likely due to a non-thermal distribution of electrons from a hybrid corona. For MAXI J1348–630, the high fraction of polarization points towards a jets origin, however, we cannot formally conclude without any infrared data giving information on the optically thin part of the synchrotron spectrum.

Key words. Accretion, accretion disks — Physical data and processes — Black hole physics — X-rays: binaries — Stars: black holes

1. Introduction

Black hole X-ray binaries are transient systems that can transit through various spectral states during their outburst. The two main states are denoted the Low Hard State (LHS) and the High Soft State (HSS; see Remillard & McClintock 2006; Belloni 2010, for a precise definition of spectral states). The LHS corresponds to the rising phase of the outburst; its 1–200 keV spectrum can be well described by a powerlaw with a photon index of $\Gamma \sim 1.5$ with an exponential cutoff usually around 100 keV. This component is usually interpreted as the emission from Compton scattering of disk photons by electrons from a hot plasma called

the “corona”. These sources are also sites of ejections of material at relativistic speeds, and sources of strong disk winds. The discovery of jets (Mirabel et al. 1992) led to name them micro-quasars. A small extension, steady “compact” jet is observed in the LHS, and has been resolved in a few sources: Cygnus X–1, GRS 1915+105, and more recently, MAXI J1348–630 (e.g., Stirling et al. 2001; Fuchs et al. 2003; Carotenuto et al. 2021). Transitions from the harder to the softer states are accompanied by transient, discrete, and large scale ejections (e.g., Fender et al. 1999; Hannikainen et al. 1999; Mirabel et al. 1998; Corbel et al. 2001; Rodriguez et al. 2008a) and no jet seems to persist in the HSS (although see Rushton et al. (2012); Zdziarski et al. (2020) for the case of Cygnus X-1). The X-ray flux in the HSS is domi-

Send offprint requests to: cangemi@apc.in2p3.fr

nated by the photon disk emission peaking at ~ 1 keV. This component is associated with a continuum usually described with a powerlaw with a photon index $\Gamma > 2.5$ and whose origin is still not yet understood.

In several sources, observations made at higher energies (> 200 keV) have revealed the presence of a high-energy non-thermal component extending up to 1 MeV (Grove et al. 1998; Cadolle Bel et al. 2006; Laurent et al. 2011; Rodriguez et al. 2015; Cangemi et al. 2021a). The origin of this high-energy emission is still not well understood and (at least) two scenarios have been invoked to explain its origin. In the first scenario, this component is the extension of the Synchrotron spectrum from the basis of the jets (Markoff et al. 2005; Laurent et al. 2011; Jourdain et al. 2014; Rodriguez et al. 2015; Kantzas et al. 2021). The alternative explanation suggests that this component arises from a non-thermal distribution of electrons in a hybrid thermal/non-thermal corona (e.g., Del Santo et al. 2013; Romero et al. 2014; Cangemi et al. 2021b,a). In the case of the high mass BHB, Cygnus X-1, Cangemi et al. (2021a) have suggested that the high-energy tails, seen both in the HSS and LHS have different origins: in the HSS an hybrid corona is favoured while the jet would be at the origin of the LHS high-energy tail.

Polarization measurements of the high-energy emission from BHBs is probably the best way to disentangle between these different scenarios as we expect distinct polarization properties between a Compton or synchrotron emission. *INTEGRAL* has already brought important insights on polarization measurements thanks to the design of the Spectrometer on board on *INTEGRAL* (SPI, Vedrenne et al. 2003) and the Imager on Board on *INTEGRAL* Satellite (IBIS; Ubertini et al. 2003) which can be used as a Compton telescope with its two layers plane (ISGRI and PICsIT). Indeed the high polarization degree of the > 400 keV Cygnus X-1 high-energy tail detected both with IBIS and SPI (Laurent et al. 2011; Jourdain et al. 2012) has been shown to be compatible with the emission of the compact jet in the LHS of this source (Rodriguez et al. 2015). Cygnus X-1 is currently the only source for which polarization measurements have been able to constrain the origin of the high-energy component. It is therefore important to look at other sources in order to probe the origin of this component and try to obtain a more general understanding of the \sim MeV emission in microquasars.

MAXI J1535–571, MAXI J1820+070 and MAXI J1348–630 are X-ray transients discovered by the Monitor of All-Sky X-ray Image (*MAXI*) on board on the International Space Station (Matsuoka et al. 2009) during their outburst in September 2017 (Negoro et al. 2017), March 2018 (Kawamuro et al. 2018) and January 2019 (Yatabe et al. 2019) respectively. The three outbursts were then followed by *INTEGRAL* (e.g., Lepingwell et al. 2018; Bozzo et al. 2018; Cangemi et al. 2019b,a) and all three sources were particularly bright and reached a maximum flux of a few Crabs. Not many other sources have reached such a brightness previously, and therefore, polarization studies on short accumulation (i.e. a few days) of data led to totally unconstrained results. Even for Cygnus X-1 the detection of polarised emission required accumulation of Ms of data over large intervals of time.

Although the mass of the compact object in MAXI J1535–571 has not been established yet, bright radio emission associated with a flat radio spectrum (Russell et al. 2017) and strong emission in the infrared band (Dinçer 2017; Vincentelli et al. 2021) led to identify the source as a BHB. The source displays strong X-ray variability, including low-frequency Quasi-Periodic Oscillations (QPOs, Stiele & Kong 2018; Huang et al. 2018; Stevens et al. 2018; Bhargava et al. 2019; Sreehari et al.

2019). MAXI J1820+070 is a X-ray binary harbouring a black hole of mass $\sim 8.5 M_{\odot}$ accreting from a companion star of $\sim 0.4 M_{\odot}$ (Torres et al. 2019, 2020). The intense brightness of the system has triggered multiple multi-wavelength observing campaigns (e.g., Bright et al. 2020; Trushkin et al. 2018; Tetarenko et al. 2021; Hoang et al. 2019) and the source was the center of many studies. MAXI J1348–630 is also a BHB with a black hole of mass $\sim 11 M_{\odot}$ (Lamer et al. 2020) and the source is located at ~ 3.3 kpc according to the measurement of Lamer et al. (2020) with *SRG/eROSITA* and *XMM-Newton* observations. The source shows also strong X-ray variability and QPOs were observed during LHS to HSS transition (Belloni et al. 2020). The source shows also a interesting behavior when looking at its radio/X-ray correlation which infers the relation between the emission from the compact jets and the inner accretion flow (Corbel et al. 2013). The correlation displays two different tracks referred as the *standard* and the *outliers* tracks. Usually, a source follows one of the tracks during its outburst, but Carotenuto et al. (2021) have shown that in the the case of MAXI J1348–630, the source follows the outliers track during the first part of the outburst before joining the standard track. Table 1 summarises all the known parameters for the three sources.

In this study, we present the evolution of the outbursts of those three different sources as observed by *INTEGRAL*. We make use of its unique capabilities in order to probe the main properties over the full 3–1000 keV range covered by the observatory. We also present polarization measurements of the high-energy component when significant emission is detected above 300 keV. The description of the observations, and the data reduction methods are reported in Sect. 2. Section 3 is dedicated to the phenomenological spectral analysis. We then present the results from our polarization measurements with the Compton mode above 300 keV for the three sources in Sect. 4. The results are finally discussed in Sect 5.

2. Data reduction

2.1. Spectral extraction: *INTEGRAL*/JEM-X

We only use data from JEM-X unit 1. The data are reduced with the OFF-LINE SCIENTIFIC ANALYSIS (OSA) version 11.1 software. We follow the standard steps described in the JEM-X user manual¹. Spectra are extracted for each Science Windows² (scw hereafter) where the source is automatically detected by the software at the image creation and fitting step. Spectra are then computed over 32 logarithmic spectral channels from ~ 3 to ~ 34 keV using the standard binning definition. Individual spectra for each period are then combined with the OSA *spe_pick* tool according to the classification scheme described in Sect. 2.4. The appropriate ancillary response files (arfs) are produced during the spectral extraction and are combined with *spe_pick*, while the redistribution matrix file (rmf) is rebinned from the instrument characteristic standard rmf with *j_rebin_rmf*. We add 3% systematic error on all spectral channels for each of the stacked spectra, as recommended in the JEM-X user manual. For our spectral analysis, we consider the spectra from 3 to 20 keV.

¹ https://www.isdc.unige.ch/integral/download/osa/doc/11.1/osa_um_jemx/man.html.

² *INTEGRAL* individual pointings of a duration of 1800–3600 s typical duration.

Table 1. Summary of the known parameters for the three studied sources.

Source	MAXI J1535–571	MAXI J1820+070	MAXI J1348–630
Mass of the black hole [M_{\odot}]	–	$8.5^{+0.8}_{-0.7}$	11^{+2}_{-2}
	–	Torres et al. (2020)	Lamer et al. (2020)
Mass of the companion [M_{\odot}]	–	$0.6^{+0.1}_{-0.1}$	–
	–	Torres et al. (2020)	–
Distance [kpc]	$4.1^{+0.6}_{-0.5}$	$3.0^{+0.3}_{-0.3}$	$3.3^{+0.3}_{-0.3}$
	Chauhan et al. (2019)	Atri et al. (2020)	Lamer et al. (2020)
Inclination [°]	$67.4^{+0.8}_{-0.8}$	63^{+3}_{-3}	28^{+3}_{-3}
	Miller et al. (2018)	Torres et al. (2020)	Anczarski et al. (2020)

2.2. Spectral extraction: INTEGRAL/IBIS/ISGRI

Data from *INTEGRAL*/IBIS upper detector ISGRI are also reduced with the *osa* 11.1 software. We use the standard procedure described in the IBIS manual³. For each scw, we create the sky model and reconstruct the sky image and the source count rates by deconvolving the shadowgrams projected onto the detector plane. For the three sources, spectra are extracted using 60 logarithmically spaced channels between 20 keV and 1000 keV. Response matrixes are automatically generated running the *osa* 11.1 spectral extraction. We then use the *spe_pick* tool to create stacked spectra for each different outburst periods (see Sect. 2.4). 2 % of systematics are added to each stacked spectra as indicated in the IBIS user manual.

2.3. Spectral extraction INTEGRAL/SPI

We followed a similar procedure already applied in the case of Cygnus X-3 (Cangemi et al. 2021b). To summarize, we use the SPI DATA ANALYSIS INTERFACE⁴ (SPIDAI) to reduce SPI data. During the outburst of MAXI J1348–630, SPI was in annealing from MJD 58501 to MJD 58522 (*INTEGRAL* revolutions 2047 to 2054), therefore we do not have available SPI data during the LHS and the IMS but we extract the SPI spectrum in the HSS. We respectively create a sky model containing MAXI J1535–571, MAXI J1820+070 and MAXI J1348–630 and set their variability to 5 scws. We then create the background model by setting the variability timescale of the normalization of the background pattern to 5 scws. Sometimes, solar flares, radiation belt entries, and other non-thermal incidents can lead to unreliable results. Therefore, we remove scws for which the reconstructed count compared to the detector counts give a poor χ^2 ($\chi^2_{\text{red}} > 1.5$) in order to avoid these effects. This selection reduces the total number of scws by $\sim 10\%$. The shadowgrams are then deconvolved to obtain the source flux, and spectra are extracted between 20 keV and 2000 keV using 27 logarithmically spaced channels. For each spectrum, we apply a correcting factor of 1/0.85 above 400 keV in order to take into account a change efficiency above this threshold (Roques & Jourdain 2019).

2.4. Data selection and period definition

We consider scw between MJD 58004–58019 (09/08/2017–09/23/2017), 58193–58249 (03/16/2018–05/11/2018) and 58512–58541 (01/29/2019–02/27/2019) respectively cor-

responding to the outburst of MAXI J1535–571, MAXI J1820+070, and MAXI J1348–630 where the sources are less than 10° off axis. Figure 1 shows the *INTEGRAL*/ISGRI lightcurves between 30 keV and 50 keV along with the *MAXI*/GSC monitoring in order to show the *INTEGRAL* observations in the long-term context of the whole outburst.

For the three sources, we perform purely phenomenological fit for each scw, in the 3–300 keV energy range using JEM-X unit 1 and ISGRI in order to separate the three datasets into different periods according to their spectral shapes and properties. The fits are performed using XSPEC (Arnaud 1996); we use a cut-off powerlaw model (CUTOFFPL) and added the emission from a disk (DISKBB) when needed. We also multiply the model with a constant (CONSTANT) allowing us to take into account calibration issues between the instruments and the differences in total exposure between the instruments⁵. Constants are let free whereas other parameters are tied between instruments.

In summary, we use CONSTANT*CUTOFFPL or CONSTANT*(CUTOFFPL+DISKBB) when high residuals are observed at low energy. Because of the low exposure of the individual spectra, we do not use absorption here, the aim being to roughly describe the shape of the spectra in order to separate the different periods of the outbursts. We then extract the values of the photon index, the exponential cutoff and the disk temperature. The evolution of these different parameters are shown in Fig. 2 for the three sources.

For MAXI J1535–571, based on the value of the photon index which transits from ~ 1.9 to ~ 2.3 from MJD 58004 to MJD 58016, we divide our datasets in two periods: the first one from 58004 to 58012 and the second one, after MJD 58016. The two periods are shown in green and orange on Fig. 1. This subdivision is consistent with the epochs defined in Russell et al. (2020) where they find that the source was in a Hard Intermediate State (HIMS) state from MJD 58008 to 58016 before its transition into a Soft Intermediate State (SIMS) at MJD 58017. Therefore, we name our two periods according to this classification.

Concerning MAXI J1820+070, the values of the photon index and the exponential cutoff are consistent with typical values observed in a LHS during all the *INTEGRAL* observations. We thus define a unique period for the characterization of this outburst. The unique period is shown in blue in Fig. 1. This is consistent with the different epochs defined in Buisson et al. (2019) where they show that the source starts its transition into the HSS around MJD 58306, after our observations.

³ https://www.isdc.unige.ch/integral/download/osa/doc/11.1/osa_um_ibis/man.html.

⁴ <https://sigma-2.cesr.fr/integral/spidai>.

⁵ Given the *INTEGRAL* observing pattern around the pointed source and since IBIS has a larger field of view than JEM-X, sources can be outside the JEM-X field of view while still in the IBIS one)

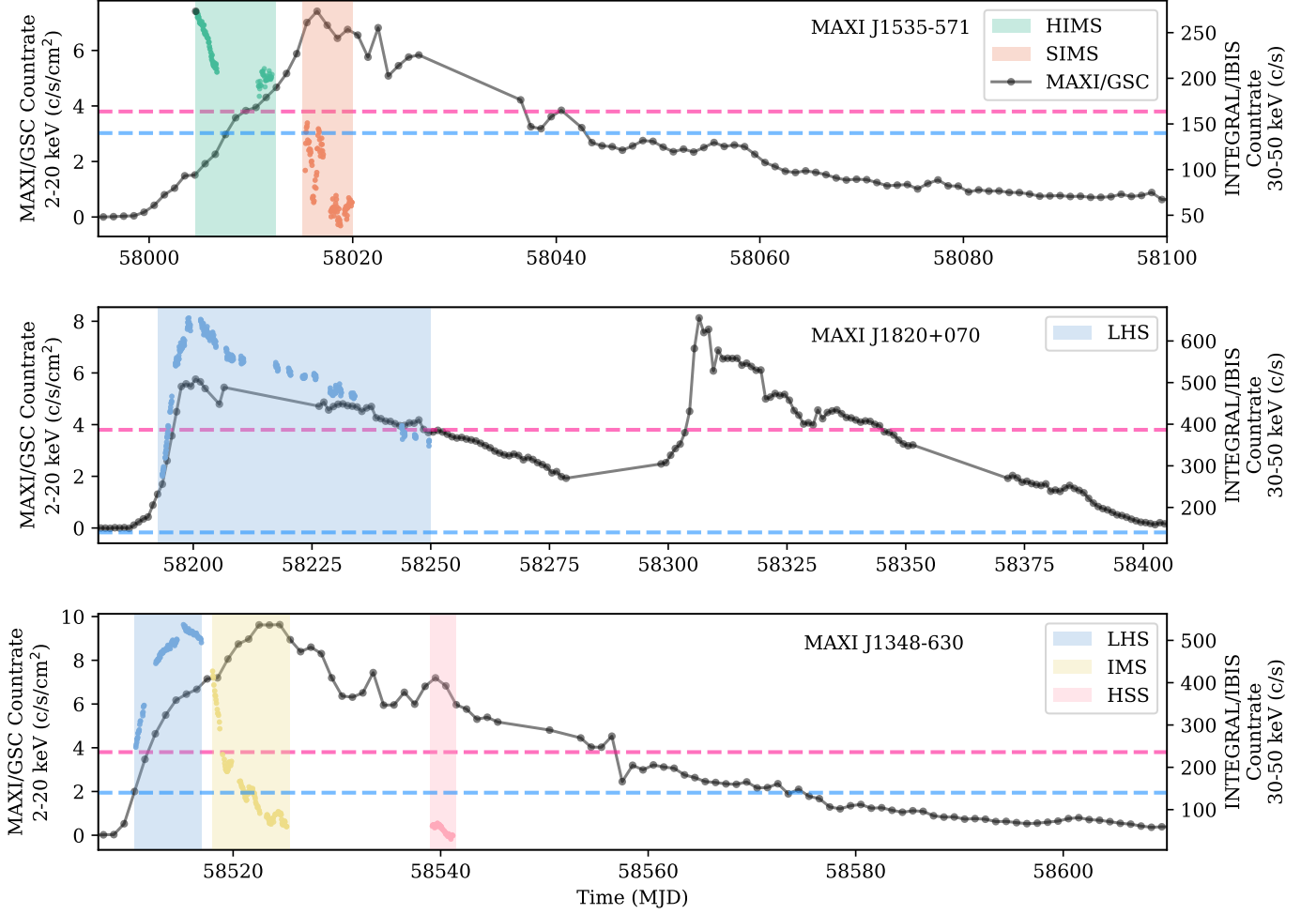


Fig. 1. *MAXI/GSC* 2–20 keV (in black) and *INTEGRAL/IBIS* 30–50 keV (colored dots) lightcurves of *MAXI* J1535–571 (top panel), *MAXI* J1820+070 (middle panel), and *MAXI* J1348–630 (bottom panel). Left and right y axis indicate the countrate for *MAXI/GSC* and *INTEGRAL/IBIS* respectively. Definitions of the different periods and the corresponding colors are described in Sect. 2.4. The counrates for 1 Crab is indicated with the pink and blue dotted lines for *MAXI/GSC* and *INTEGRAL/IBIS*, respectively.

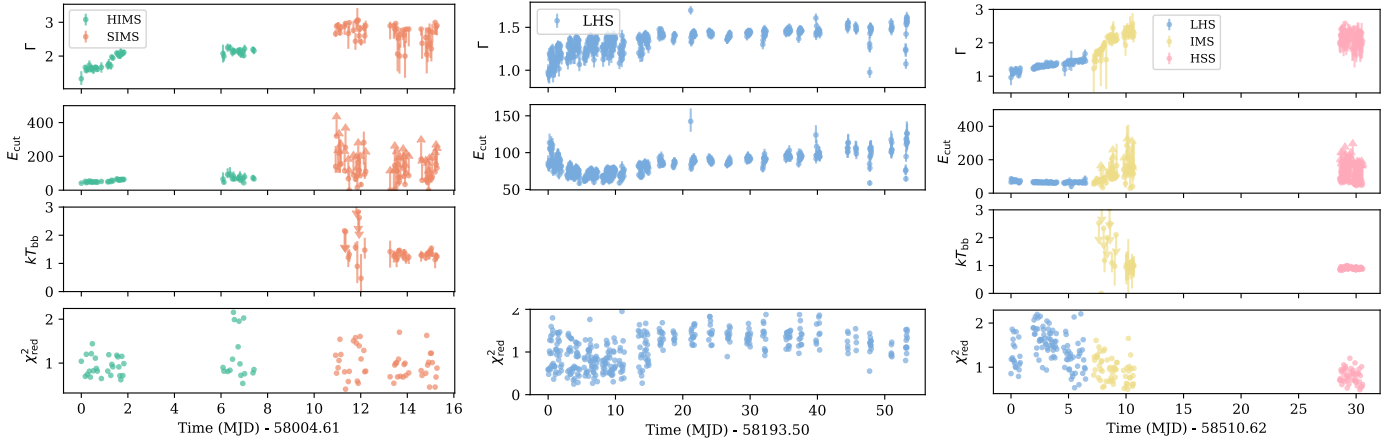


Fig. 2. Temporal evolution of the different spectral parameters extracted from our phenomenological spectral fitting for *MAXI* J1535–571 (left panel), *MAXI* J1820+070 (middle panel), and *MAXI* J1348–630 (right panel). Definitions of the different periods and their corresponding colors are described in Sect. 2.4

The study of the *MAXI* J1348–630 spectral evolution shows two changes in the spectral shape. The first change occurs around MJD 58517 where we observe an increase of the photon in-

dex from ~ 1.6 to 2.3 and an increase of the cutoff energy from 50 keV to above detection threshold. We define these two periods as the LHS (in blue of Fig. 1) and InterMediate State (IMS,

in yellow on Fig. 1) states. Here we are not able to identify the different flavors (HIMS and SIMS) of the IMS. The observations from the last period, after MJD 58539, show a higher photon index value ~ 2.3 associated with a high-energy exponential cut-off, not constrained in the majority of our observations (see the lower limits on Fig 2). Belloni et al. (2020) find a similar state classification when analysing data from *NICER*. Figure 1 shows the LHS, IMS and HSS state periods in blue, yellow and pink, respectively.

The broadband *INTEGRAL* spectra are shown on Fig. 3. The different state spectra are plotted with different colors using the same color code as in Fig. 1.

3. State dependent spectral analysis

3.1. Methodology

According to the state classification described in Sect. 2.4, we have different stacked spectra for different periods of the three outbursts. In order to assess the potential presence of a high-energy tail in a state-resolved way, we follow the same methodology described in Cangemi et al. (2021b,a). This methodology is divided in two steps: we first analyse the data from 3 to 100 keV with a reflected (REFLECT, Magdziarz & Zdziarski 1995) thermal Comptonization continuum (NTHCOMP, Zdziarski et al. 1996). We also add the iron line at 6.4 keV with a Gaussian (GAUSSIAN). Although, the reflection is not needed in the individual spectra, it is needed in the stacked spectra in order to obtain a statistically good fit. We choose this Comptonization model rather than another because the MAXI J1820+070 spectrum is better fitted with this model than with other thermal Comptonization models we have tested (e.g., COMPTT). This model has also been used by Shidatsu et al. (2019) to fit *MAXI/GSC* and *Swift/BAT* data of MAXI J1820+070. For the sake of consistency, we also use NTHCOMP for MAXI J1535–571 and MAXI J1348–630. We also add the absorption by the interstellar medium (TBABS, Wilms et al. 2000) using ANGR solar abundances (Anders & Ebihara 1982). The model is written `CONSTANT*TBABS*(REFLECT(NTHCOMP) + GAUSSIAN)` in XSPEC. We add the emission from a disk (DISKBB, Mitsuda et al. 1984) when needed. In this case, the model becomes `CONSTANT*TBABS*(REFLECT(NTHCOMP) + DISKBB + GAUSSIAN)`. We let the energy of the iron line vary between 6.2 keV to 6.5 keV whereas its width is allowed to vary between 0.2 keV to 0.5 keV. Once we obtain a satisfactory fit, we add the data above 100 keV, let the parameters vary freely and search for presence of residuals at high-energy. In case of large residuals observed above 300 keV, we add a powerlaw component (`CONSTANT*TBABS*(REFLECT(NTHCOMP) + GAUSSIAN + POWERLAW)` or `CONSTANT*TBABS*(REFLECT(NTHCOMP) + DISKBB + GAUSSIAN + POWERLAW)`) to the model and investigate the significance of this component by performing a F-test. We use an inclination of $i = 67^\circ$ (Miller et al. 2018), 63° (Torres et al. 2019), and 28° (Anczarski et al. 2020) for the reflection component for MAXI J1535–571, MAXI J1820+070 and MAXI J1348–630 respectively. The reflection fraction is allowed to vary between $0 < \Omega/2\pi < 2$.

The best-fit parameters obtained in the 3–2000 keV band are reported in Tab. 2 and the corresponding spectral fits for each source in the different states are shown in Fig. 4. If the addition of a disk is necessary to fit the data, we indicate “yes” in the row called “Disk”. Rows “Flux” and “Flux_{po}” respectively refer to the flux given by the total model and the flux which comes from an additional powerlaw component in the 300–1000 keV range.

3.2. Results

3.2.1. MAXI J1535–571

During the HIMS, the seed-photon energy is unconstrained, we thus fix its value to 0.3 keV according to e.g., Sridhar et al. (2019), Tao et al. (2018). The value for the density column $n_H \sim 3.3 \times 10^{22} \text{ cm}^{-2}$ is consistent with the value measured by Sridhar et al. (2019) (*Astrosat*) but it is slightly lower compared to the value obtained by Xu et al. (2018) (*NuSTAR*). This difference can arise by the use of slightly different epochs of observations between the different analysis. Moreover, Xu et al. (2018) attribute their high value ($n_H \sim 8 \times 10^{22} \text{ cm}^{-2}$) to the inclusion of the thermal disk in their modelling. The electron temperature of $kT \sim 52 \text{ keV}$ we obtain is consistent with results from Sridhar et al. (2019) and Tao et al. (2018). We find a photon index of the Comptonized continuum rather soft $\Gamma_{th} \sim 2.38$ slightly higher than that found in the different modelizations of Sridhar et al. (2019) and a reflection fraction of $\Omega/2\pi \sim 1.1$. During the SIMS, we observe residuals below $\sim 10 \text{ keV}$ and we add a disk to model the corresponding spectra. The disk temperature is tied to the photon seed temperature of NTHCOMP. We find $kT_0 \sim 1.24 \text{ keV}$ in agreement with the value obtained by Tao et al. (2018). The other parameters are roughly the same as in the SIMS except for $\Gamma_{th} \sim 2.52$ for which we observe a slight increase. Our best fit gives a lower limit of > 1.8 for the reflection fraction. We have tested other reflection model like RELXILL which also give a similarly large reflection fraction. In their study, Miller et al. (2018) have tested different reflection models, and notably RELXILL and RELLINE and also obtain a large reflection fraction. Following these authors such large value is compatible with an X-ray source very close to the black hole, the large reflection then being due to the strong expected light bending. Our results agree with their best fit parameters. We will not enter in more details of the reflection component here since it is not the main subject of this paper.

Interestingly, we need an additional powerlaw component for both states in order to model the spectra above 300 keV. For the HIMS, inclusion of the powerlaw improves χ_{red}^2 from 155.95/93 dof to $\chi_{red}^2 = 112.45/91$ dof; for the SIMS, it is improved from $\chi_{red}^2 = 292.30/94$ dof to $\chi_{red}^2 = 133.88/92$ dof. The photon index Γ_{po} of this powerlaw is consistent between the two periods, and we find $\Gamma_{po}^{HIMS} = 2.1_{-0.5}^{+0.4}$ and $\Gamma_{po}^{SIMS} = 2.0_{-0.4}^{+0.4}$. We observe that the flux $> 300 \text{ keV}$ is dominated by this additional component. In order to assess the existence of this powerlaw component, we also try to fit the data using solely a powerlaw instead of the thermal Comptonization model. In this case, the data is poorly represented ($\chi_{red}^2^{HIMS} = 490.53/94$ dof and $\chi_{red}^2^{SIMS} = 210.15/95$ dof), and we observe strong residuals in the 30–50 keV range clearly indicating the presence of a cutoff in this energy range.

3.2.2. MAXI J1820+070

In MAXI J1820+070, the value of the density column is unconstrained, thus, we fix it according to the value $n_H = 1.4 \times 10^{21}$ obtained by Kajava et al. (2019). We find a Comptonized continuum rather hard with a photon index of $\Gamma_{th} \sim 1.61$ and an electron energy $kT \sim 57 \text{ keV}$. Our value for the electron energy is higher compared to the value found by Zdziarski et al. (2021), $kT \sim 12 \text{ keV}$, which use the data above 20 keV from ISGRI and SPI and the 3–80 keV data from *NuSTAR*. However, they use a

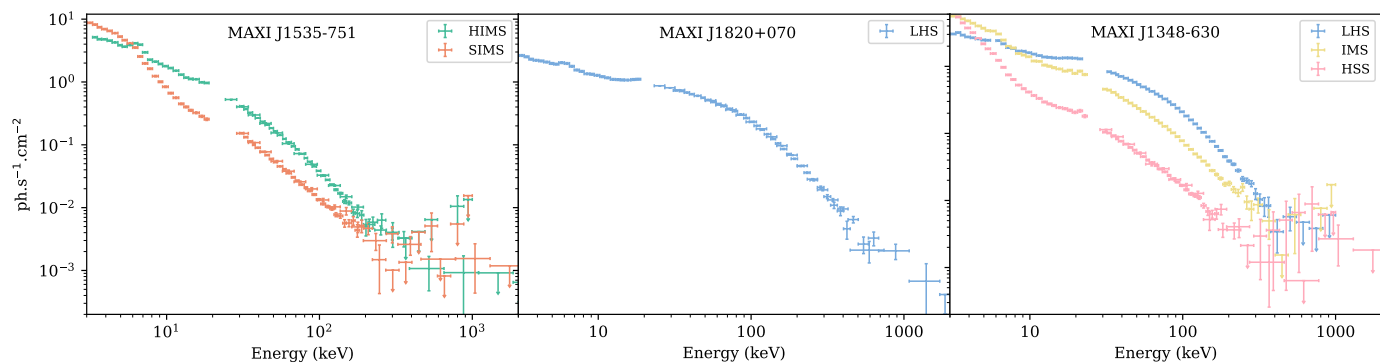


Fig. 3. Stacked spectra extracted from JEM-X, ISGRI and SPI for MAXI J1535–571 (left panel), MAXI J1820+070 (middle panel), and MAXI J1348–630 (right panel). The different color indicates the different epochs considered using the same color code as in Fig. 1.

Table 2. Parameters obtained for our phenomenological fitting for each source and each period.

Parameters	MAXI J1535–571		MAXI J1820+070	MAXI J1348–630		
	HIMS	SIMS	LHS	LHS	IMS	HSS
C_{ISGRI}	$0.93^{+0.04}_{-0.03}$	$1.14^{+0.01}_{-0.02}$	$0.91^{+0.03}_{-0.02}$	$0.82^{+0.03}_{-0.02}$	$0.8^{+0.2}_{-0.2}$	$0.85^{+0.04}_{-0.04}$
C_{SPI}	$0.90^{+0.04}_{-0.03}$	$1.20^{+0.01}_{-0.02}$	$0.91^{+0.03}_{-0.02}$	–	–	$0.90^{+0.04}_{-0.04}$
$n_{\text{H}} [\times 10^{22} \text{ cm}^{-2}]$	$3.3^{+0.6}_{-0.7}$	2.5^{+1}_{-1}	0.14 F	0.86 F	0.86 F	0.86 F
$kT_0 [\text{keV}]$	0.3 F	$1.24^{+0.04}_{-0.03}$	0.2 F	0.5 F	$1.21^{+0.09}_{-0.08}$	$0.84^{+0.03}_{-0.03}$
$kT [\text{keV}]$	52^{+43}_{-17}	40^{+106}_{-26}	57^{+4}_{-4}	44^{+5}_{-4}	> 193	> 471
$\Omega/2\pi$	$1.1^{+0.8}_{-0.3}$	> 1.8	> 1	$0.8^{+0.1}_{-0.1}$	$1.0^{+0.2}_{-0.1}$	$0.46^{+0.09}_{-0.08}$
$E_{\text{Fe}} [\text{keV}]$	$6.5^{+0.0}_{-0.1}$	$6.2^{+0.3}_{-0.0}$	$6.2^{+0.3}_{-0.0}$	$6.20^{+0.02}_{-0.00}$	$6.20^{+0.09}_{-0.00}$	$6.2^{+0.3}_{-0.00}$
$\sigma_{\text{Fe}} [\text{keV}]$	$0.5^{+0.0}_{-0.2}$	$0.2^{+0.3}_{-0.0}$	$0.5^{+0.0}_{-0.3}$	$0.5^{+0.0}_{-0.2}$	0.4 F	$0.5^{+0.0}_{-0.2}$
Γ_{th}	$2.38^{+0.05}_{-0.09}$	$2.52^{+0.08}_{-0.09}$	$1.61^{+0.01}_{-0.01}$	$1.69^{+0.04}_{-0.03}$	$2.06^{+0.03}_{-0.03}$	$2.19^{+0.02}_{-0.02}$
Γ_{po}	$2.1^{+0.4}_{-0.5}$	$2.0^{+0.4}_{-0.4}$	$2.09^{+0.03}_{-0.03}$	$2.0^{+0.3}_{-0.3}$	–	–
Disk	no	yes	no	yes	yes	yes
Flux 300–1000 keV [$\times 10^{-9} \text{ ergs cm}^{-2} \text{ s}^{-1}$]	1.6	1.6	5.6	5.6	0.9	0.2
Flux _{po} 300–1000 keV [$\times 10^{-9} \text{ ergs cm}^{-2} \text{ s}^{-1}$]	1.6	1.6	4.6	5.3	–	–
χ^2/dof	112.45/91	133.88/92	88.68/75	62.56/68	110.18/72	135.67/95

modified version of `COMPBS`⁶ as their thermal description of the continuum and this could explain the difference compared to our study. The value we find for the electron temperature is also roughly consistent with the work of Chakraborty et al. (2020) and Buisson et al. (2019) where they combine *NuSTAR* and *Astrosat* data. They both use a two coronal component model and find $kT \sim 38 \text{ keV}$ when tying the two corona temperature components. We do not add a disk component to the model and we fix the photon seed energy to $kT_0 = 0.2 \text{ keV}$ (e.g., Wang et al. 2020; Dziełak et al. 2021). We find a reflection fraction $\Omega/2\pi > 1$.

When adding the data above 300 keV, the addition of a powerlaw to the model strongly improve the goodness of the fit (from $\chi^2_{\text{red}} = 367.23/77 \text{ dof}$ to $\chi^2_{\text{red}} = 88.68/75 \text{ dof}$). We observe that the $> 300 \text{ keV}$ is largely dominated by the emission from this high-energy component (82% of the 300–1000 keV flux).

3.2.3. MAXI J1348–630

The parameter n_{H} is unconstrained and we fix its value to $n_{\text{H}} = 8.6 \times 10^{21} \text{ cm}^{-2}$ (Tominaga et al. 2020). Parameters found in LHS are very close to those found during the outburst of MAXI

J1820+070. We obtain a photon index $\Gamma_{\text{th}} \sim 1.69$ and an electron energy $kT \sim 44 \text{ keV}$. It is mentioned that a black body component is present in the LHS (e.g., Tominaga et al. 2020; Chakraborty et al. 2020; Zhang et al. 2021) with a temperature of $\sim 0.5 \text{ keV}$. At such a temperature, the flux of the disk could contribute $> 3 \text{ keV}$ and therefore we add a `DISKBB` component in our model. The normalization of this component is fixed to 12000, value found by Chakraborty et al. (2020). Strong residuals are observed at high energy when fitting solely with `CONST*(REFLECT(NTHCOMP) + GAUSS)`. The addition of a powerlaw component improves χ^2_{red} from 112.42/70 dof to 62.56/68 dof. We find a photon index of $\Gamma_{\text{po}} = 2.0$ and measure a reflection fraction of ~ 0.8 .

We also use a disk to model the IMS and the HSS. As for the states of MAXI J1535–571, the flux at low energy is dominated by the disk emission. The photon disk energy is slightly higher during the IMS than during the HSS. Using *NICER* and *Astrosat*, Zhang et al. (2021) and Jithesh et al. (2021) find a consistent value analysing data from different observations made during the HSS. However, Zhang et al. (2021) observe a higher value of Γ_{th} (~ 3.3) than observed during both periods corresponding to our HIMS and SIMS. Note that we also model those two periods with a simple reflected powerlaw and a disk (`REFLECT(POWERLAW)`

⁶ They use a sinusoidal distribution of the seed photons in a sphere.

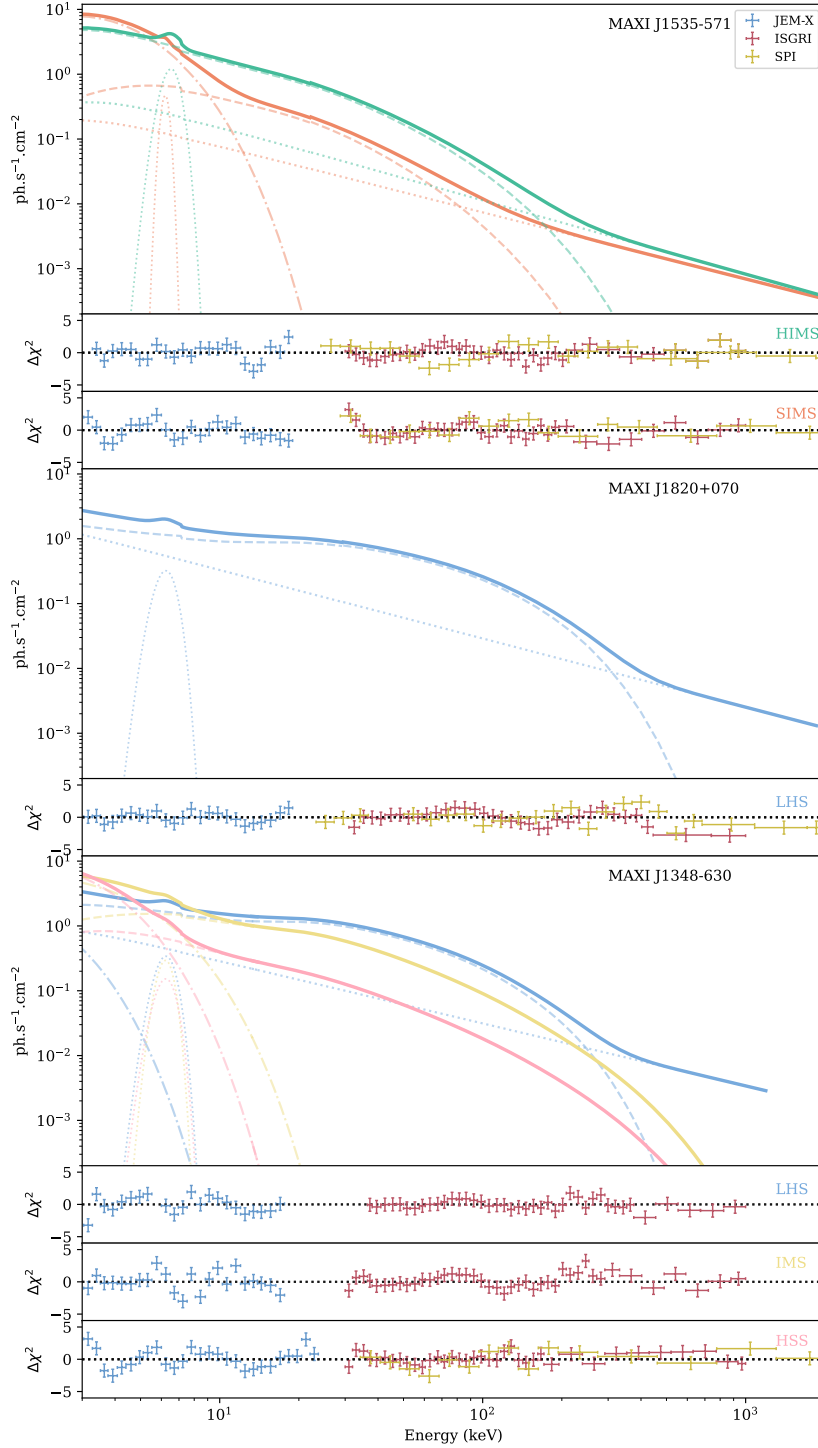


Fig. 4. Best-fit models obtained from our phenomenological fitting of the 3–2000 keV for MAXI J1535–571 (top panel), MAXI J1820+070 (middle panel), and MAXI J1348–630 (bottom panel). Different colors indicate different epochs using the same color code as in Fig. 1. JEM-X, ISGRI and SPI data are represented with blue, red and yellow respectively. Residuals for each period are plotted separately at the bottom of the corresponding spectrum. Different model components are shown with different line styles: Comptonized continuum, (dashed), disk (dotted-dashed), additional powerlaw (densely dotted), gaussian (dotted).

+ DISKBB + GAUSSIAN). In this case, we do not find a satisfactory fit for the IMS ($\chi_{\text{red}}^2 = 248.13/75$), but the HSS can be well described by this purely phenomenological model and parameters are consistent with the previous modelization.

4. Polarization with the Compton mode

4.1. Principle of the Compton Mode

Thanks to its two layer detectors; ISGRI at the top and the Pixelated Imaging Caesium Iodide Telescope (PICsIT, Labanti et al. 2002) at the bottom, IBIS can be used as a Compton polarimeter.

This concept relies on the cross section $d\sigma$ which represents the probability for a polarized photon with an energy E_1 to enter in interaction with an electron from the detector (e.g., Evans & Beiser 1956):

$$\frac{d\sigma}{d\Omega} = \frac{r_0^2}{2} \left(\frac{E_2}{E_1} \right)^2 \left(\frac{E_2}{E_1} + \frac{E_1}{E_2} - 2 \sin^2 \theta_c \cos^2 \phi \right) \quad (1)$$

where E_2 is the energy of the scattered photon in the solid angle $d\Omega$, θ_c is the scatter angle, r_0 is the electron radius and ϕ is the azimuthal angle of the scattered photon with respect to the polarization direction (see e.g., Fig. 1 of Forot et al. 2007). Using the relation between E_1 and E_2 :

$$\frac{E_1}{E_2} = \frac{1}{1 + \frac{E_2}{m_e c^2} (1 - \cos \theta_c)} \quad (2)$$

we note that for a fixed scattered angle, the cross section will be maximal for $\phi = \pi/2 + k\pi$ with $k \in \mathbb{Z}$. This creates an asymmetry in the number of detected photons by PICsIT. We can evaluate the detected photon distribution on the PICsIT detector with respect to the azimuth ϕ :

$$N(\phi) = C[1 + a_0 \cos(2(\phi - \phi_0))] \quad (3)$$

where C is the mean count rate. Then we can deduce the polarization angle $PA = \phi_0 - \pi/2$ and the polarization fraction Π :

$$\Pi = \frac{a_0}{a_{100}} \quad (4)$$

where a_{100} represents the amplitude of a 100% polarized source (Suffert et al. 1959). The value of a_{100} depends on several factors as the detector dimension, the detection threshold, the level of noise etc. In the case of IBIS, we simulate the emission from a monochromatic source for which we apply the same treatment as for a real source. The resulting modulation is used to deduce the value of a_{100} for this energy. We then weight this value by the source spectrum and obtain the value of a_{100} for the desired energy band. It is usually around 0.2–0.3 depending on the considered energy band (Laurent et al. 2011; Rodriguez et al. 2015). Figure A.1 shows the evolution of a_{100} as a function of the energy.

In order to measure $N(\phi)$, we need to select the simple Compton events, i.e. those for which photons interact only once in ISGRI and once in PICsIT. ‘‘Spurious events’’ are removed according to the method described in Forot et al. (2007). Photons are accumulated in six different angle ranges of 30° each. In order to improve the signal to noise ratio in each channel, we take advantage of the π symmetry of the differential cross section described by equation (1) since e.g., the first channel contains photons with an azimuth $0^\circ < \phi < 30^\circ$ and photons with an azimuth $180^\circ < \phi < 210^\circ$. Shadowgrams are formed for each channel angle chosen by the user, then deconvolved and count rates are extracted.

The uncertainty on $N(\phi)$ is dominated by statistical fluctuations, since our observations are background dominated. Therefore, confidence intervals for ϕ_0 and a_0 are not derived by a $N(\phi)$ fit to the data but obtained with a Bayesian approach following the work of Forot et al. (2008) and described in Vaillancourt (2006) and Weisskopf et al. (2006). In this computation, we suppose that all real polarization angles and fractions have a uniform probability distribution (non-informative prior densities, Quinn 2012; Maier et al. 2014) and that the real polarization angle and

fraction are ϕ_0 and a_0 . We then need the probability density distribution of measuring a and ϕ from N_{pt} independent data points in $N(\phi)$ during a period π , which is given by (Vaillancourt 2006; Forot et al. 2008; Maier et al. 2014) :

$$dP(a, \phi) = \frac{N_{\text{pt}} C^2}{\pi \sigma_C^2} \exp \left[-\frac{N_{\text{pt}} C^2}{2 \sigma_C^2} [a^2 + a_0^2 - 2aa_0 \cos(2\phi - 2\phi_0)] \right] a da d\phi \quad (5)$$

where σ_C is the uncertainty of C . Uncertainties of a and ϕ can then be deduced by integrating $dP(a, \phi)$ by respect to the other dimension. We emphasize that this probability is a conditional probability and is calculated by supposing that the emission is indeed polarized.

There are also several systematics uncertainties that arise from measurements of polarization with a Compton telescope using a coded mask. The non-axisymmetric geometry of the detectors and the systematics due to the analysis process have been studied in details in Forot et al. (2008). We also study the modulation from the background by selecting events from detector pixels hidden from the source by opaque mask elements, for scws of MAXI J1820+070. We find a modulation of 5% for the different energy bands used in the analysis. All these systematics uncertainties are taken into account in the derivation of the polarization constrains measured in this paper.

4.2. Results

Figure 5 shows polarigrams in the 300–1000 keV band for the different periods of the three sources, following the same color code as in Fig. 1. Figures A.3 and A.4 show polarigrams in the 300–1000 keV and 400–1000 keV bands respectively. Polarigrams are fitted with a constant (dashed grey line) and the sinusoid function described in equation (3) (colored line). During the LHS periods of MAXI J1820+070 and MAXI J1348–630, we also show in Fig. 6 the integrated probability function described by equation (5) in function of the polarization angle ϕ and the polarization fraction Π . Other probability density functions are shown on Fig. A.2. Table 3 summarizes the different parameters we measure for the three sources and for three different energy bands: 300–400 keV, 400–1000 keV and 300–1000 keV. We indicate the total effective exposure time, the signal to noise ratio, the a_{100} value, the χ_{red}^2 obtained by fitting $N(\phi)$ by a constant (C) or by the sinusoid function (S) described by equation (3), the polarization angle PA and the polarization fraction Π . Note that we use a range of 0 – 180° for our fitting. Uncertainties represent an interval confidence of 67%. The last column indicates whether polarization is detected (\checkmark) or not (\times). We consider that polarization is detected by validating two conditions: (1) we need a signal to noise ratio higher than 12 to obtain reliable results; this value is based on empirical results on the Crab (Laurent et al. 2016), and (2) the probability p_{unpola} of measuring modulation knowing that the source is unpolarized is $< 1\%$. All p_{unpola} are shown in Table 3 (only for polarigrams where the signal to noise ratio is higher than 12).

We do not detect polarization for MAXI J1535–571. Indeed, for both states and for the three energy bands, the signal to noise ratio is too poor and no modulation is detected.

The diagnosis is different for MAXI J1820+070. Indeed, for the three considered energy bands, polarigrams show clear deviation from a constant which poorly represents the data. We find a much better description of the data with the sine function (eq. 3).

Table 3. Parameters obtained for our polarization analysis using the Compton mode. C and S is the value of the χ^2_{red} obtained using a constant (C) or a sinusoidal (S) function for our polarigram fit.

Source	State period	Exposure time [Ms]	Energy band	Signal to noise ratio	a_{100}	χ^2/dof	p_{unpol} [%]	Polarization Angle [°]	Polarization fraction [%]	Polarization detected
MAXI J1535–571	HIMS	0.22	300–400 keV	4.9	0.278	C = 2.35/5 S = 1.52/4	–	–	–	×
			400–1000 keV	7.2	0.194	C = 1.30/5 S = 0.64/4	–	–	–	×
			300–1000 keV	8.7	0.224	C = 1.35/5 S = 0.92/4	–	–	–	×
	SIMS	0.16	300–400 keV	3.3	0.278	C = 8.00/5 S = 5.60/4	–	–	–	×
			400–1000 keV	3.7	0.194	C = 2.00/5 S = 2.72/4	–	–	–	×
			300–1000 keV	4.9	0.224	C = 6.35/5 S = 6.40/4	–	–	–	×
MAXI J1820+070	LHS	1.3	300–400 keV	71	0.278	C = 12.05/5 S = 6.44/4	0.57	120 ± 14	17 ± 8	✓
			400–1000 keV	67	0.194	C = 13.1/5 S = 4.48/4	0.11	105 ± 11	35 ± 12	✓
			300–1000 keV	94	0.224	C = 20.65/5 S = 7.44/4	0.003	110 ± 11	26 ± 9	✓
MAXI J1348–630	LHS	0.32	300–400 keV	22.9	0.278	C = 12.30/5 S = 0.84/4	0.02	160 ± 9	75 ± 26	✓
			400–1000 keV	22	0.194	C = 9.40/5 S = 5.28/4	0.06	180 ± 10	> 70	✓
			300–1000 keV	30.7	0.224	C = 15.45/5 S = 0.68/4	0.008	180 ± 10	79 ± 23	✓
	IMS	0.17	300–400 keV	8.2	0.278	C = 13.15/5 S = 12.84/4	–	–	–	×
			400–1000 keV	7.2	0.194	C = 4.95/5 S = 3.88/4	–	–	–	×
			300–1000 keV	10.42	0.224	C = 7.45/5 S = 6.32/4	–	–	–	×
	HSS	0.42	300–400 keV	2.79	0.278	C = 3.15/5 S = 0.48/4	–	–	–	×
			400–1000 keV	3.01	0.194	C = 11.01/5 S = 4.08/4	–	–	–	×
			300–1000 keV	4.12	0.224	C = 5.55/5 S = 1.32/4	–	–	–	×

In the three energy bands, we calculate the probability given by equation (eq. 5) using the values of a and ϕ we find in our best fit. Figure 6 (left) shows the contour plot we obtain in the 300–1000 keV bands; polarization is detected with a interval confidence higher than 99 %, and we find a polarization angle and a polarization fraction consistent with $PA \sim 110^\circ$ and $\Pi \sim 25\%$ in the three energy bands.

Concerning MAXI J1348–630, polarigrams extracted from the IMS and HSS periods have poor signal to noise ratio. On the other hand, polarigrams from the LHS period have sufficient signal to noise to probe the presence of a modulation. We find that polarigrams are poorly described by a constant and $p_{\text{unpol}} < 1\%$ in the different energy bands. We then calculate the probability (eq. 5) to measure the polarization angle PA and a polarization fraction Π . The contour plot is shown on Fig. 6 (right). We find lower limits for the polarization fraction of 49 %, 70 % and 56 % with a polarization angle of $\sim 160^\circ$, $\sim 180^\circ$ and $\sim 180^\circ$ for the 300–400 keV, 300–1000 keV and 300–1000 keV bands respectively.

5. Discussion and interpretation

5.1. Summary of the results

5.1.1. MAXI J1535–571

We separate the data in two intervals corresponding to a HIMS and SIMS, which respectively match epochs defined in Russell et al. (2020). In both periods, the source spectra are rather soft and characterized by a photon index $\Gamma_{\text{th}}^{\text{HIMS}} = 2.38^{+0.05}_{-0.09}$ and $\Gamma_{\text{th}}^{\text{SIMS}} = 2.52^{+0.08}_{-0.09}$. The low energy emission starts to be dominated by the accretion disk during the SIMS period and its en-

ergy temperature peaks at $kT_0 = 1.24^{+0.04}_{-0.03}$ keV which is a typical value usually observed in soft states of BHBs (e.g., Remillard & McClintock 2006). The energy from the corona electrons is not well defined in both states with a value greater than 50 keV.

We detect an additional component above the Comptonization bump during both states. This high-energy component is described by a powerlaw with a photon index of $\Gamma_{\text{po}}^{\text{HIMS}} = 2.1^{+0.4}_{-0.5}$ and $\Gamma_{\text{po}}^{\text{SIMS}} = 2.0^{+0.4}_{-0.4}$.

Using the Compton mode, we do not detect polarization in either both states. We remark, however, that the source flux above 300 keV is quite low (see Table 2) resulting in a poor signal to noise ratio for our polarization measurements. The non-detection is compatible with this empirical minimum value to obtain a trustworthy detection of signal. Therefore, we cannot conclude for MAXI J1535–571 if the lack of polarization detection at high energy is an intrinsically characteristic of the source or an observational issue.

5.1.2. MAXI J1820+070

MAXI J1820+070 is the brightest of the three sources observed in the ISGRI 30–50 keV range. The source is observed during its LHS (e.g., Buisson et al. 2019). The spectrum is characterized by a hard photon index $\Gamma_{\text{th}} = 1.61^{+0.01}_{-0.01}$ and corona electron energy of 57^{+4}_{-4} keV. An additional powerlaw component clearly improves the fit and we find a photon index of $\Gamma_{\text{po}} = 2.09^{+0.03}_{-0.03}$. This component strongly dominates the spectrum above 300 keV with a flux of 4.6×10^{-9} erg s $^{-1}$ cm $^{-2}$.

Polarigrams extracted in the 300–400 keV, 400–1000 keV and 300–1000 keV show a strong modulation of the signal and we measure a 300–1000 keV polarization fraction of $\Pi = 26 \pm 9$

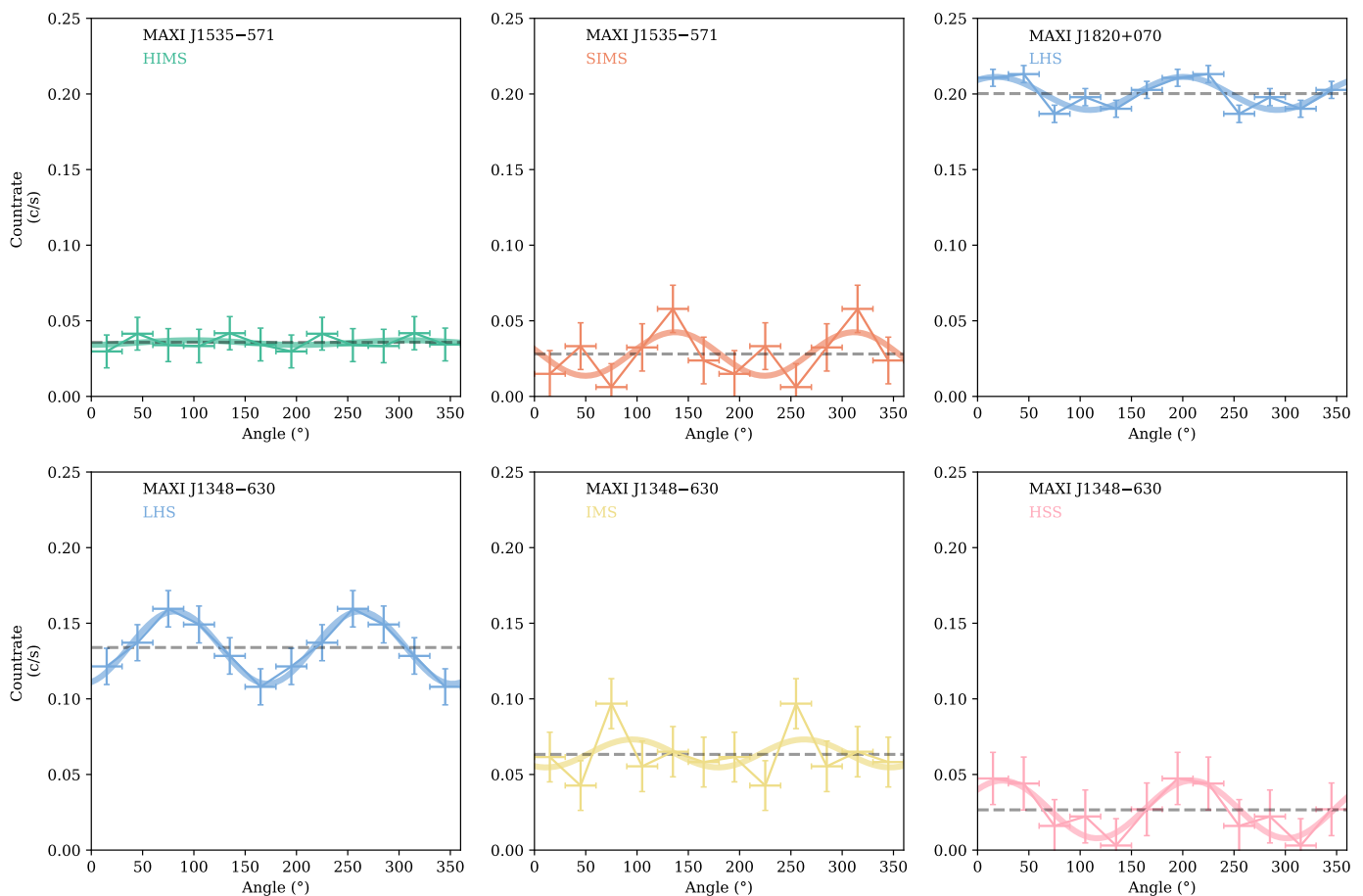


Fig. 5. Polarigrams of the three sources obtained in the 300–1000 keV energy band range.

and a polarization angle $PA = 110 \pm 11^\circ$ (see Tab. 3 for the energy dependent results), errors are given in a 67 % confidence range.

5.1.3. MAXI J1348–630

We follow the evolution of the source during its outburst and identify three different periods corresponding to three different states of the source, LHS, IMS and HSS. During its LHS, we find a photon index of $\Gamma_{\text{th}} = 1.69^{+0.04}_{-0.03}$ and an electron energy $kT = 44^{+5}_{-4}$ keV. We detect an additional powerlaw component with a photon index of $\Gamma_{\text{po}} = 2.0^{+0.3}_{+0.3}$.

While a high-energy tail is clearly present in the LHS, no high-energy component is detected in either of the softer states. Consistently polarization can be probed only in the LHS, and we indeed detect the same polarization angle $PA = 180 \pm 10^\circ$ for the 400–1000 keV and 300–1000 keV bands. This value is not strictly consistent with the value of $PA = 160 \pm 9^\circ$ we measure in the 300–400 keV band, but it is consistent at 90 % confidence ($PA = 160 \pm 30^\circ$). This slight discrepancy could arise from some contribution of the Comptonized continuum, as the 300–400 keV range is not purely described by the additional powerlaw. We measure a high polarization fraction for the three energy bands with a lower limit $> 70\%$ for the 400–1000 keV. The other energy bands allows lower polarization fractions; $\Pi^{300-400\text{keV}} > 49\%$ and $\Pi^{300-1000\text{keV}} > 56\%$.

5.2. Origin of the high-energy emission

We detect a powerlaw tail in addition to the standard Comptonisation component during the HIMS and SIMS of MAXI J1535–571, the LHS of MAXI J1820+070 and during the LHS of MAXI J1348–630. This component is strongly present at the beginning of the outburst when the global spectral shape is hard and its strength decays as the outburst evolves to softer states. There are two obvious possibilities for the “apparent” absence of high-energy tails in softer states. Either 1) the emission genuinely vanishes; 2) the high-energy emission falls below detection threshold.

Case 1) implies that the medium responsible for the high-energy component disappears in the softer states. One obvious candidate is the compact jet, which is known to be quenched in the HSS (e.g., Fender et al. 1999), and was claimed to emit in the 400–2000 keV range in Cygnus X-1 (Laurent et al. 2011; Jourdain et al. 2012; Rodriguez et al. 2015). Since ejections of coronae state transitions have been proposed in other sources (e.g., Rodriguez et al. 2008a,b), the corona would also be a good candidate. Case 2) implies an evolution of the high-energy component parameters (at least its flux) which also leads to at least two interpretations. 2a) Same medium with evolving properties, e.g., in Cygnus X-3, the tails seems un-related to the jets behavior, and well explained by an hybrid corona in all states (Cangemi et al. 2021b). 2b) Different emitting media, as observed in Cygnus X-1 (Cangemi et al. 2021a). In the case of Cygnus X-1, we note that the jets origin in both states could also be a possibility (Zdziarski et al. 2020).

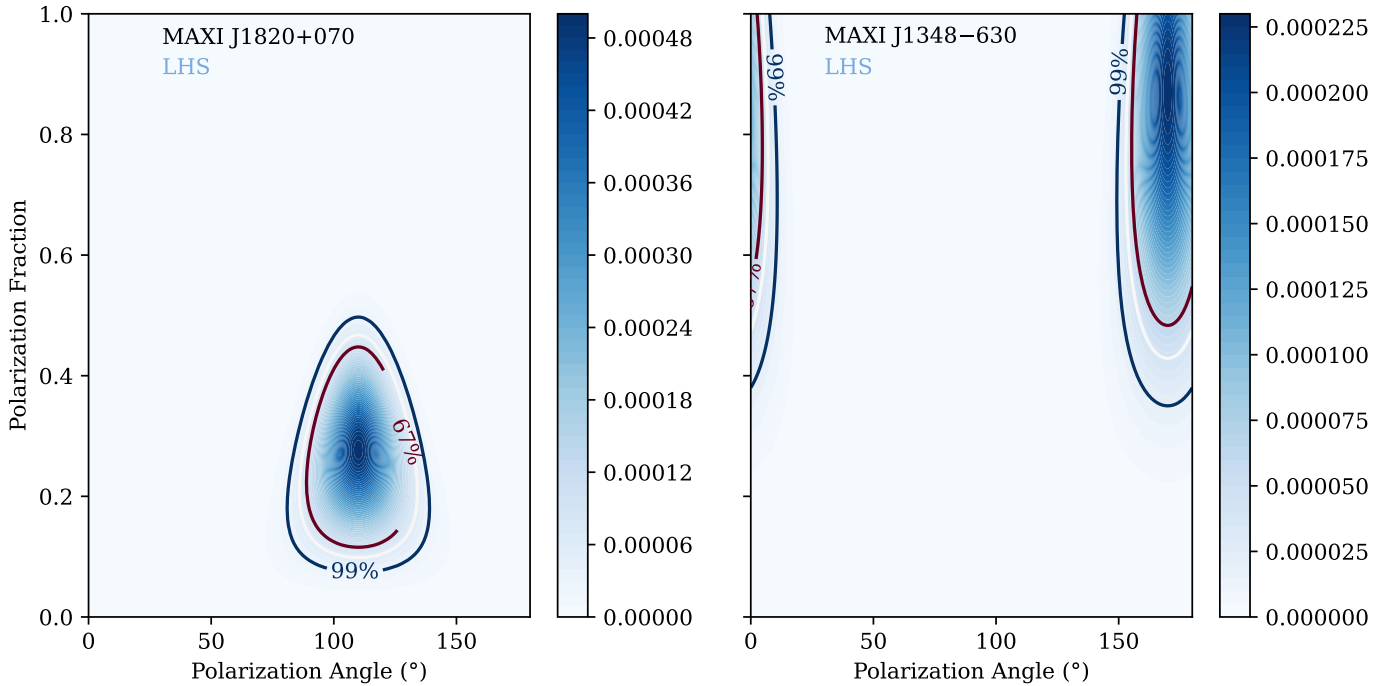


Fig. 6. Probability density described by equation (5) in function of the polarization angle and the polarization fraction calculated for MAXI J1820+070 (left) and MAXI J1348–630 in the LHS (right).

Polarization is an additional diagnostic to constrain the origin of the tail. The synchrotron spectrum of a population of N electrons with an energy between E and $E + dE$ and with an electron index p , $dN(E) \propto E^{-p}dE$ can be approximated by a powerlaw $P(E) \propto E^{-\alpha}$. The spectral index α and the electron index p are tied by the equation $\alpha = (p - 1)/2$ (Rybicki & Lightman 1986) and α can also be related to the photon index Γ : $\alpha = \Gamma - 1$. In a very ordered magnetic field, the polarization fraction of a polarized emission expected in the optically thin regime of the synchrotron spectrum, is (Rybicki & Lightman 1986):

$$\Pi = \frac{p + 1}{p + \frac{7}{3}} \quad (6)$$

In the case of MAXI J1348–630, the value of the photon index during the LHS $\Gamma_{po} = 2.0^{+0.3}_{-0.3}$ leads to a polarization fraction of $\Pi = 75^{+11}_{-11}\%$ which is consistent with the polarization fraction observed in the three energy bands considered. Therefore, the observed emission could arise from the synchrotron emission from the jets base in a very ordered magnetic field. Besides, synchrotron emission from compact radio jets has been observed during the LHS of MAXI J1348–630 (e.g., Russell et al. 2020; Carotenuto et al. 2021).

While the upper limit (or non-detection) in the case of MAXI J1535–571 does not allow to conclude, the case of MAXI J1820+070 is quite interesting. The rather low level of polarization (compared to MAXI J1348–630 and Cygnus X-1) may indicate various possibilities. Here the measured value of the photon index $\Gamma_{po} = 2.09^{+0.03}_{-0.03}$ leads to a polarization fraction of $75 \pm 2\%$ not consistent with the polarization fraction we measure. This could indicate (1) the magnetic field is disrupted by some mechanism and/or different jet zones emits polarized radiation with different angles; or (2) another origin than the jets for the polarized emission.

5.3. SEDs basic analysis

While a precise spectral modelisation with physical models is beyond the scope of this paper, we can apply a simple approach using spectral energy distribution to verify the jet hypothesis. Here, the goal is to investigate whether the optically thin part of the synchrotron spectrum from the jets is consistent with our measured high-energy component. Therefore, we need the information on the synchrotron break frequency of the jets spectrum as well as the spectral index of the optically thin part. Then, we can extrapolate the synchrotron spectrum up to 1 MeV and check the consistency with the hard X-rays.

5.3.1. MAXI J1535–571

Figure 7 shows different datasets from Russell et al. (2020) in the HIMS (green) and in the SIMS (orange). The grey line indicates the energy of the synchrotron break, whereas the green line is the optically thin part of the synchrotron spectrum obtained by Russell et al. (2020) ($\alpha = 0.83 \pm 0.09$, where α is the spectral index of the optically thin part of the synchrotron spectrum), extrapolated up to 1000 keV. We also show the spectra extracted in this work and their associated powerlaws. The box on the top right corner of the figure is an enlarged view from 100 keV to 1000 keV. We observe that the extrapolation of the optically thin spectrum is consistent, within the errorbars, with the powerlaw in the HIMS. This could point towards a jets origin of the high-energy component in this state. However, the uncertainties are large at high energy, and without polarization measurements, we cannot exclude a hybrid corona origin. Concerning the SIMS, Russell et al. (2020) shows that the radio emission is quenched in this state. Therefore, the non-thermal component > 200 keV in this state could come from another region from the jets that still radiates in the X-ray or has another origin.

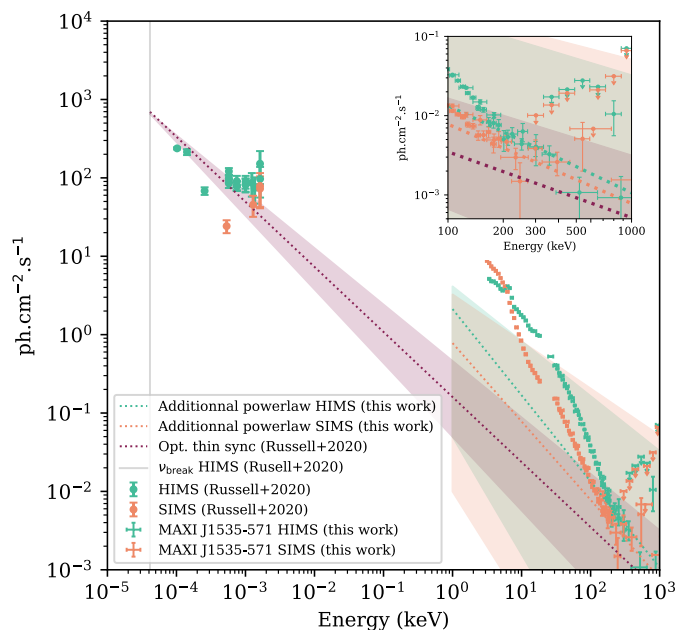


Fig. 7. MAXI J1535–571 spectra using observational data from Russell et al. (2020) and this work. HIMS and SIMS data are represented in green and orange, respectively. The measured additional high-energy components are indicated with dotted line. Their 90% uncertainties interval range are represented by the colored area. The purple dotted line is the extrapolation of the optically thin synchrotron spectrum from Russell et al. (2020) with $\alpha = 0.83 \pm 0.09$.

5.3.2. MAXI J1820+070

The dotted green line on Fig. 8 shows the extrapolation of the optically thin synchrotron spectrum measured with simultaneous (12th of april 2018) X-*Shooter* data (green dots Rodi et al. 2021). The X-ray spectrum from this work is shown with blue dots whereas the dotted blue line shows our measured powerlaw. Here, the IR optically thin spectrum is not consistent with the high-energy component that we measure. This result clearly excludes a pure synchrotron jets origin for the additional component and favours a hybrid corona origin as proposed by Zdziarski et al. (2021). Regarding our polarization measurements, a polarization fraction of $26 \pm 9\%$ is also consistent with a hybrid corona origin (Beheshtipour et al. 2017).

5.3.3. MAXI J1348–630

No infrared data has been published on MAXI J1348–630 so far. Therefore, we do not have informations on the synchrotron cutoff. However, we try to investigate the consistency of the high-energy emission detected with synchrotron emission from the jets assuming a spectral index $-0.5 < \alpha < 0.8$, a flux $40 < F < 300$ mJy at the synchrotron cutoff energy 1.5×10^{15} Hz. Figure 9 shows the resulting broad band spectrum. We also plot the optically thick part of the synchrotron spectrum as measured by Carotenuto et al. (2021) with ATCA at MJD 58514.01.

As we add a disk to model the spectrum (see Sect. 3), we investigate the impact of the black body disk normalization value on the powerlaw normalization and photon index values. We let the normalization parameter of DISKBB vary from 1×10^4 to 2×10^4 which is the upper limit obtained by Chakraborty et al. (2020). The resulting powerlaws from the fit are shown in different colors on Fig. 9 and the insert is an enlarged view from 1 keV to 1000 keV. The normalization of the black body disk has a strong

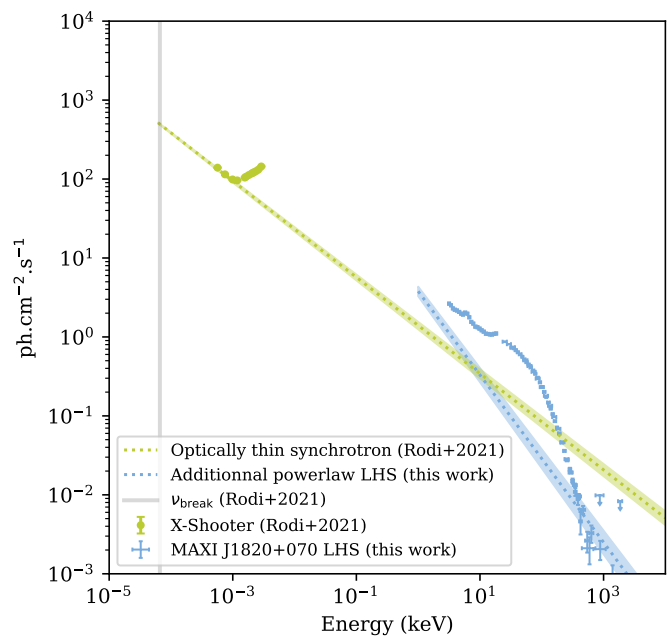


Fig. 8. MAXI J1820+070 spectrum using observational data from Rodi et al. (2021) and this work. The measured additional high-energy component is indicated with the blue dotted line. The green dotted line is the extrapolation of the optically thin synchrotron spectrum from Rodi et al. (2021).

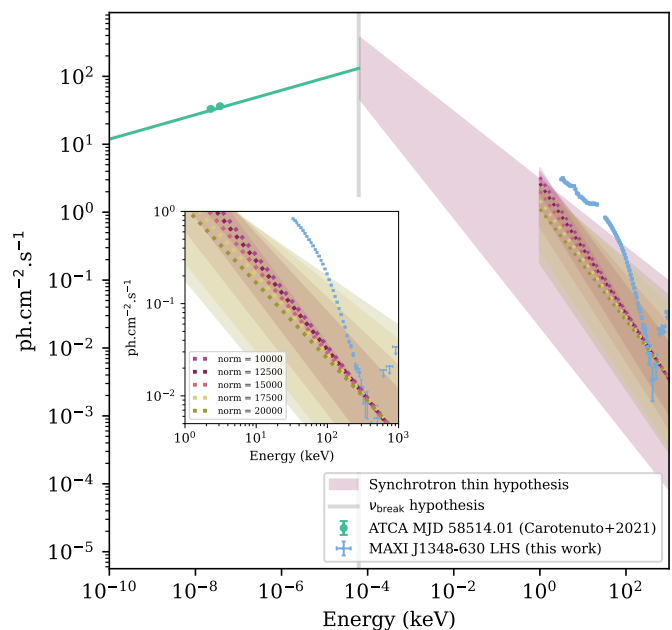


Fig. 9. Broad band spectrum of MAXI J1348–630. The light blue line is the spectrum as measured by Carotenuto et al. (2021). The green zone corresponds to our synchrotron thin spectrum hypothesis (see the text). The insert plot focus on the 1–1000 keV range. The different colors indicates the resulting powerlaw for different normalization value of the DISKBB.

impact on the powerlaw properties and we note that for normalization higher than ~ 15000 , the powerlaw component is consistent with the purple zone and therefore with the synchrotron scenario. However, although the high polarization fraction is also consistent with synchrotron emission, our synchrotron hypothesis also strongly depends on the energy of the synchrotron break,

and we cannot formally conclude for a synchrotron origin without any precise measurement of the optically thin part of the synchrotron spectrum.

6. Summary and conclusion

In this work, we use the *INTEGRAL* unique capabilities to investigate the high-energy properties of three sources, MAXI J1535–571, MAXI J1820+070, MAXI J1348–630 during their outburst. For each outburst, we divide the data into different state periods based on their spectral characteristics. Thanks to the combination of JEM-X, ISGRI and SPI data, we create stacked spectra in the 3–2000 keV band range for each of these states. We then use a simple phenomenological spectral approach in order to investigate the behavior of the sources at high-energy and search for an additional high-energy component.

We use the Compton mode of *INTEGRAL*/IBIS to study polarization properties and find that the 300–1000 keV emission from the LHS of MAXI J1820+070 and MAXI J1348–630 are polarized.

We extrapolate the optically thin part observed in the IR of the synchrotron spectrum to investigate the potential origin of the high-energy component detected in these sources. In the HIMS of MAXI J1535–571, the synchrotron spectrum is consistent with the detected high-energy component. However, we could not measure polarization in this source and therefore cannot exclude a hybrid corona origin. For MAXI J1820+070, the extrapolation of the synchrotron spectrum is not consistent with the extension measured in the X-rays. Therefore the non-thermal component could arise from a non-thermal distribution of electron from the corona. The polarization fraction that we measure is also consistent with this scenario. In the case of the high-energy component detected in the LHS of MAXI J1348–630, the high polarization fraction we measure is consistent with synchrotron emission in a very ordered magnetic field. However, we prefer not to conclude on the origin of the high-energy component without any clear information on the optically thin part of the synchrotron spectrum.

Acknowledgements. J.R., P.L. P.-O.P & C.G. acknowledge partial funding from the French Space Agency (CNES). J.R. & P.-O.P acknowledge partial fundings from the French Programme National des Hautes Energies (PNHE). T.M.B. acknowledges financial contribution from the agreement ASI-INAF n. 2017-14-H.0 and from PRIN INAF 2019 n.15. Based on observations with *INTEGRAL*, an ESA project with instruments and science data centre funded by ESA member states (especially the PI countries: Denmark, France, Germany, Italy, Switzerland, Spain) and with the participation of Russia and the USA.

References

Anczarski, J., Neilsen, J., Remillard, R., et al. 2020, in American Astronomical Society Meeting Abstracts, Vol. 235, American Astronomical Society Meeting Abstracts #235, 369.02

Anders, E. & Ebihara, M. 1982, *Meteoritics*, 17, 180

Arnaud, K. A. 1996, in *Astronomical Society of the Pacific Conference Series*, Vol. 101, *Astronomical Data Analysis Software and Systems V*, ed. G. H. Jacoby & J. Barnes, 17

Atri, P., Miller-Jones, J. C. A., Bahramian, A., et al. 2020, *MNRAS*, 493, L81

Beheshtipour, B., Krawczynski, H., & Malzac, J. 2017, *ApJ*, 850, 14

Belloni, T. M. 2010, *States and Transitions in Black Hole Binaries*, ed. T. Belloni, Vol. 794, 53

Belloni, T. M., Zhang, L., Kylafis, N. D., Reig, P., & Altamirano, D. 2020, *MNRAS*, 496, 4366

Bhargava, Y., Belloni, T., Bhattacharya, D., & Misra, R. 2019, *MNRAS*, 488, 720

Bozzo, E., Savchenko, V., Ferrigno, C., et al. 2018, *The Astronomer’s Telegram*, 11478, 1

Bright, J. S., Fender, R. P., Motta, S. E., et al. 2020, *Nature Astronomy*, 4, 697

Buisson, D. J. K., Fabian, A. C., Barret, D., et al. 2019, *MNRAS*, 490, 1350

Cadolle Bel, M., Sizun, P., Goldwurm, A., et al. 2006, *A&A*, 446, 591

Cangemi, F., Belloni, T., & Rodriguez, J. 2019a, *The Astronomer’s Telegram*, 12471, 1

Cangemi, F., Beuchert, T., Siegert, T., et al. 2021a, *A&A*, 650, A93

Cangemi, F., Rodriguez, J., Belloni, T., Clavel, M., & Grinberg, V. 2019b, *The Astronomer’s Telegram*, 12457, 1

Cangemi, F., Rodriguez, J., Grinberg, V., et al. 2021b, *A&A*, 645, A60

Carotenuto, F., Corbel, S., Tremou, E., et al. 2021, *MNRAS*, 504, 444

Chakraborty, S., Navale, N., Ratheesh, A., & Bhattacharyya, S. 2020, *MNRAS*, 498, 5873

Chauhan, J., Miller-Jones, J. C. A., Anderson, G. E., et al. 2019, *MNRAS*, 488, L129

Corbel, S., Coriat, M., Brocksopp, C., et al. 2013, *MNRAS*, 428, 2500

Corbel, S., Kaaret, P., Jain, R. K., et al. 2001, *ApJ*, 554, 43

Del Santo, M., Malzac, J., Belmont, R., Bouchet, L., & De Cesare, G. 2013, *MNRAS*, 430, 209

Dinçer, T. 2017, *The Astronomer’s Telegram*, 10716, 1

Dzielać, M. A., De Marco, B., & Zdziarski, A. A. 2021, *MNRAS*, 506, 2020

Evans, R. D. & Beiser, A. 1956, *Physics Today*, 9, 33

Fender, R., Corbel, S., Tzioumis, T., et al. 1999, *ApJ*, 519, L165

Forot, M., Laurent, P., Grenier, I. A., Gouiffès, C., & Lebrun, F. 2008, *ApJ*, 688, L29

Forot, M., Laurent, P., Lebrun, F., & Limousin, O. 2007, *ApJ*, 668, 1259

Fuchs, Y., Rodriguez, J., Mirabel, I. F., et al. 2003, *A&A*, 409, L35

Grove, J. E., Johnson, W. N., Kroeger, R. A., et al. 1998, *ApJ*, 500, 899

Hannikainen, C. D., Hunstead, W. R., Durouchoux, P., et al. 1999, *Astrophysical Letters and Communications*, 38, 237

Hoang, J., Molina, E., Lopez, M., et al. 2019, in *International Cosmic Ray Conference*, Vol. 36, 36th International Cosmic Ray Conference (ICRC2019), 696

Huang, Y., Qu, J. L., Zhang, S. N., et al. 2018, *ApJ*, 866, 122

Jithesh, V., Misra, R., Maqbool, B., & Mall, G. 2021, *MNRAS*, 505, 713

Jourdain, E., Roques, J. P., & Chauvin, M. 2014, *ApJ*, 789, 26

Jourdain, E., Roques, J. P., Chauvin, M., & Clark, D. J. 2012, *ApJ*, 761, 27

Kajava, J. J. E., Motta, S. E., Sanna, A., et al. 2019, *MNRAS*, 488, L18

Kantzas, D., Markoff, S., Beuchert, T., et al. 2021, *MNRAS*, 500, 2112

Kawamuro, T., Negoro, H., Yoneyama, T., et al. 2018, *The Astronomer’s Telegram*, 11399, 1

Labanti, C., Di Cocco, G., Malaguti, G., et al. 2002, *Nuclear Instruments and Methods in Physics Research A*, 477, 561

Lamer, G., Schwobe, A. D., Predehl, P., et al. 2020, *arXiv e-prints*, arXiv:2012.11754

Laurent, P., Gouiffès, C., Rodriguez, J., & Chambouleyron, V. 2016, in 11th *INTEGRAL Conference Gamma-Ray Astrophysics in Multi-Wavelength Perspective*, 22

Laurent, P., Rodriguez, J., Wilms, J., et al. 2011, *Science*, 332, 438

Lepingwell, V. A., Bazzano, A., Bird, A. J., et al. 2018, *The Astronomer’s Telegram*, 11884, 1

Magdziarz, P. & Zdziarski, A. A. 1995, *MNRAS*, 273, 837

Maier, D., Tenzer, C., & Santangelo, A. 2014, *PASP*, 126, 459

Markoff, S., Nowak, M. A., & Wilms, J. 2005, *ApJ*, 635, 1203

Matsuoka, M., Kawasaki, K., Ueno, S., et al. 2009, *PASJ*, 61, 999

Miller, J. M., Gendreau, K., Ludlam, R. M., et al. 2018, *ApJ*, 860, L28

Mirabel, I. F., Dhawan, V., Chaty, S., et al. 1998, *A&A*, 330, L9

Mirabel, I. F., Rodriguez, L. F., Cordier, B., Paul, J., & Lebrun, F. 1992, *Nature*, 358, 215

Mitsuda, K., Inoue, H., Koyama, K., et al. 1984, *PASJ*, 36, 741

Negoro, H., Ishikawa, M., Ueno, S., et al. 2017, *The Astronomer’s Telegram*, 10699, 1

Quinn, J. L. 2012, *A&A*, 538, A65

Remillard, R. A. & McClintock, J. E. 2006, *ARA&A*, 44, 49

Rodi, J., Tramacere, A., Onori, F., et al. 2021, *ApJ*, 910, 21

Rodriguez, J., Grinberg, V., Laurent, P., et al. 2015, *ApJ*, 807, 17

Rodriguez, J., Hannikainen, D. C., Shaw, S. E., et al. 2008a, *ApJ*, 675, 1436

Rodriguez, J., Shaw, S. E., Hannikainen, D. C., et al. 2008b, *ApJ*, 675, 1449

Romero, G. E., Vieyro, F. L., & Chaty, S. 2014, *A&A*, 562, L7

Roques, J.-P. & Jourdain, E. 2019, *ApJ*, 870, 92

Rushton, A., Miller-Jones, J. C. A., Campana, R., et al. 2012, *MNRAS*, 419, 3194

Russell, T. D., Lucchini, M., Tetarenko, A. J., et al. 2020, *MNRAS*, 498, 5772

Russell, T. D., Miller-Jones, J. C. A., Sivakoff, G. R., Tetarenko, A. J., & Jacpot Xrb Collaboration. 2017, *The Astronomer’s Telegram*, 10711, 1

Rybicki, G. B. & Lightman, A. P. 1986, *Radiative Processes in Astrophysics*

Shidatsu, M., Nakahira, S., Murata, K. L., et al. 2019, *ApJ*, 874, 183

Sreehari, H., Ravishankar, B. T., Iyer, N., et al. 2019, *MNRAS*, 487, 928

Sridhar, N., Bhattacharyya, S., Chandra, S., & Antia, H. M. 2019, *MNRAS*, 487, 4221

Stevens, A. L., Uttley, P., Altamirano, D., et al. 2018, *ApJ*, 865, L15

Stiele, H. & Kong, A. K. H. 2018, *ApJ*, 868, 71

Stirling, A. M., Spencer, R. E., de la Force, C. J., et al. 2001, *MNRAS*, 327, 1273

- Suffert, M., Endt, P. M., & Hoogenboom, A. M. 1959, *Physica*, 25, 659
- Tao, L., Chen, Y., Güngör, C., et al. 2018, *MNRAS*, 480, 4443
- Tetarenko, A. J., Casella, P., Miller-Jones, J. C. A., et al. 2021, *MNRAS*, 504, 3862
- Tominaga, M., Nakahira, S., Shidatsu, M., et al. 2020, *ApJ*, 899, L20
- Torres, M. A. P., Casares, J., Jiménez-Ibarra, F., et al. 2020, *ApJ*, 893, L37
- Torres, M. A. P., Casares, J., Jiménez-Ibarra, F., et al. 2019, *ApJ*, 882, L21
- Trushkin, S. A., Nizhelskij, N. A., Tsybulev, P. G., & Erkenov, A. 2018, *The Astronomer's Telegram*, 11539, 1
- Ubertini, P., Lebrun, F., Di Cocco, G., et al. 2003, *A&A*, 411, L131
- Vaillancourt, J. E. 2006, *PASP*, 118, 1340
- Vedrenne, G., Roques, J. P., Schönfelder, V., et al. 2003, *A&A*, 411, L63
- Vincentelli, F. M., Casella, P., Russell, D. M., et al. 2021, *MNRAS*, 503, 614
- Wang, Y., Ji, L., Zhang, S. N., et al. 2020, *ApJ*, 896, 33
- Weisskopf, M. C., Elsner, R. F., Hanna, D., et al. 2006, arXiv e-prints, astro
- Wilms, J., Allen, A., & McCray, R. 2000, *ApJ*, 542, 914
- Xu, Y., Harrison, F. A., García, J. A., et al. 2018, *ApJ*, 852, L34
- Yatabe, F., Negoro, H., Nakajima, M., et al. 2019, *The Astronomer's Telegram*, 12425, 1
- Zdziarski, A. A., Johnson, W. N., & Magdziarz, P. 1996, *MNRAS*, 283, 193
- Zdziarski, A. A., Jourdain, E., Lubiński, P., et al. 2021, *ApJ*, 914, L5
- Zdziarski, A. A., Shapopi, J. N. S., & Pooley, G. G. 2020, *ApJ*, 894, L18
- Zhang, L., Altamirano, D., Uttley, P., et al. 2021, *MNRAS*, 505, 3823

Appendix A: Additional figures

..

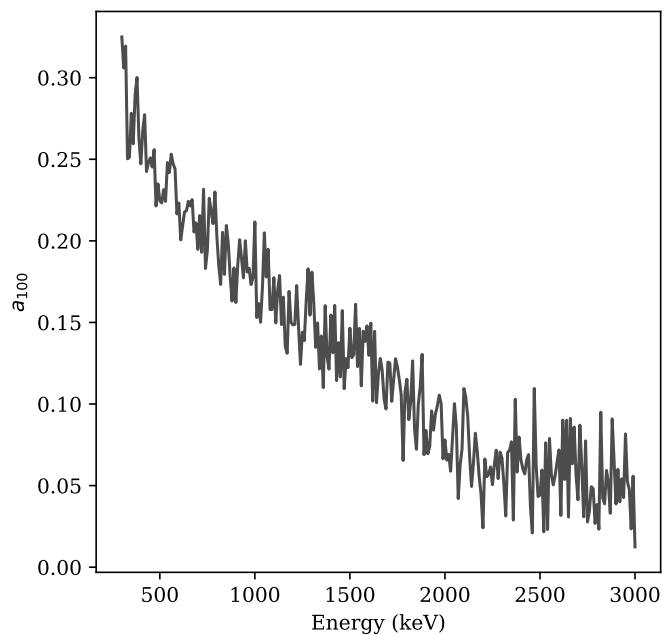


Fig. A.1. Evolution of the modulation parameter a_{100} as a function of the energy.

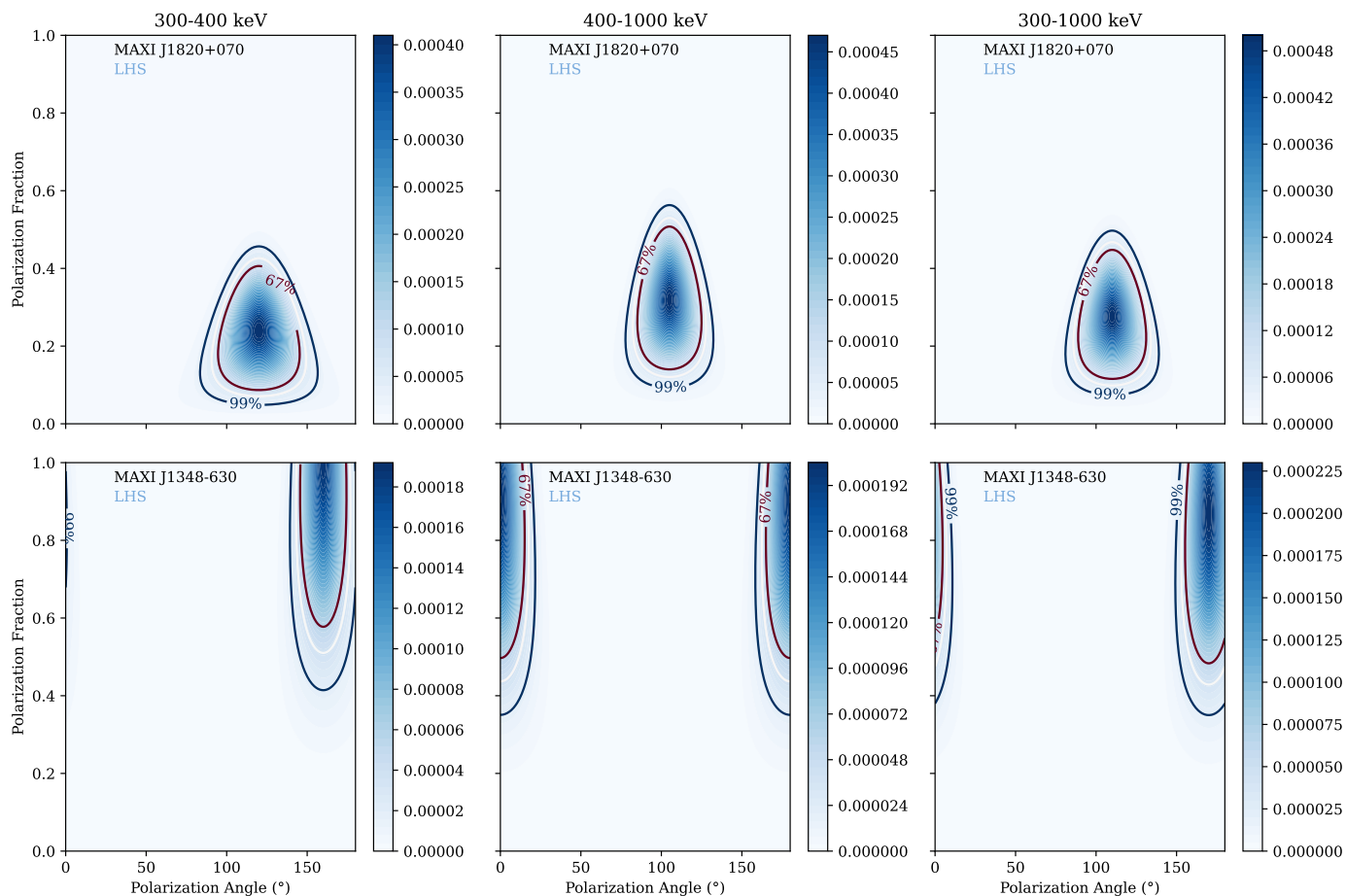


Fig. A.2. Probability density described by equation (5) in function of the polarization angle and the polarization fraction calculated for MAXI J1820+070 (top) and MAXI J1348–630 (bottom) in the LHS for different energy bands.

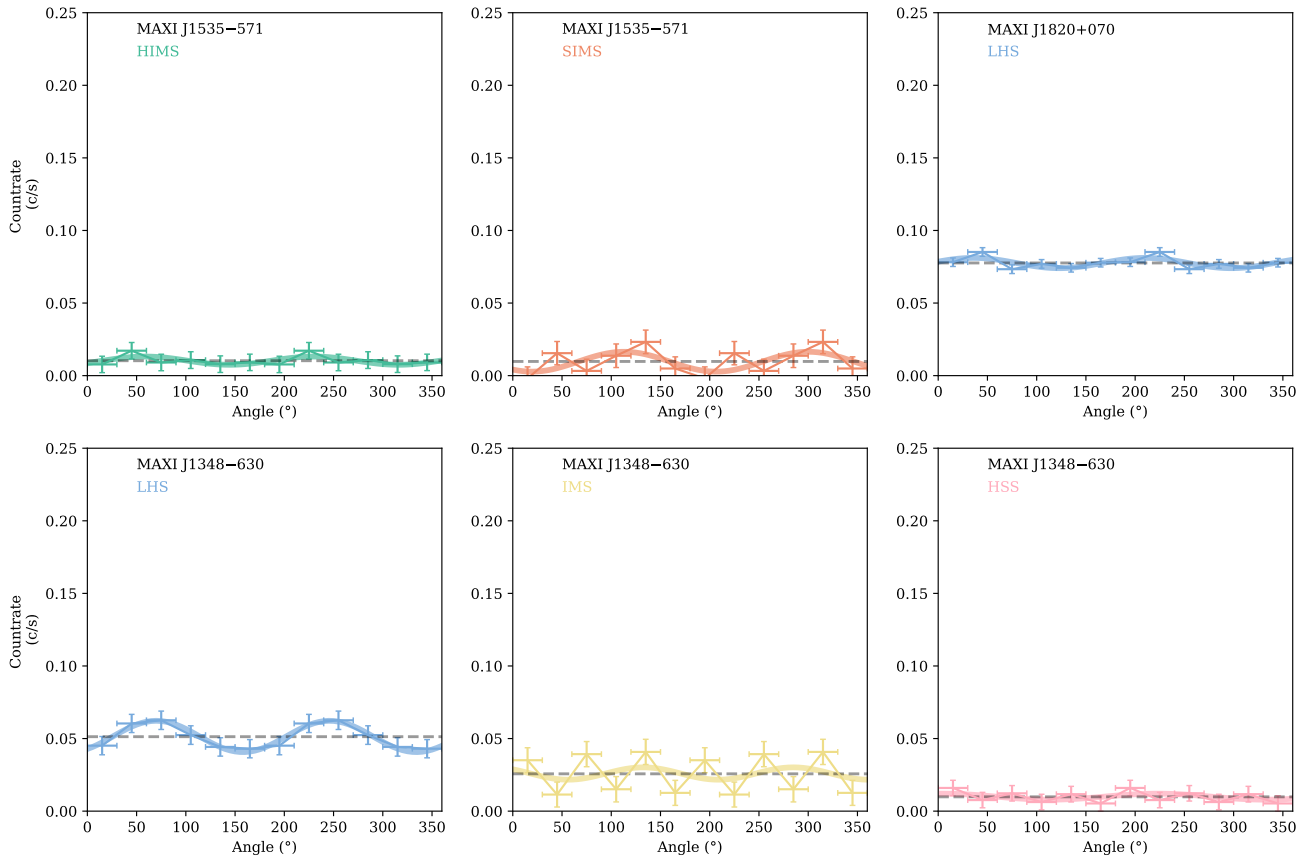


Fig. A.3. Polarigrams of the three sources obtained in the 300–400 keV energy band range.

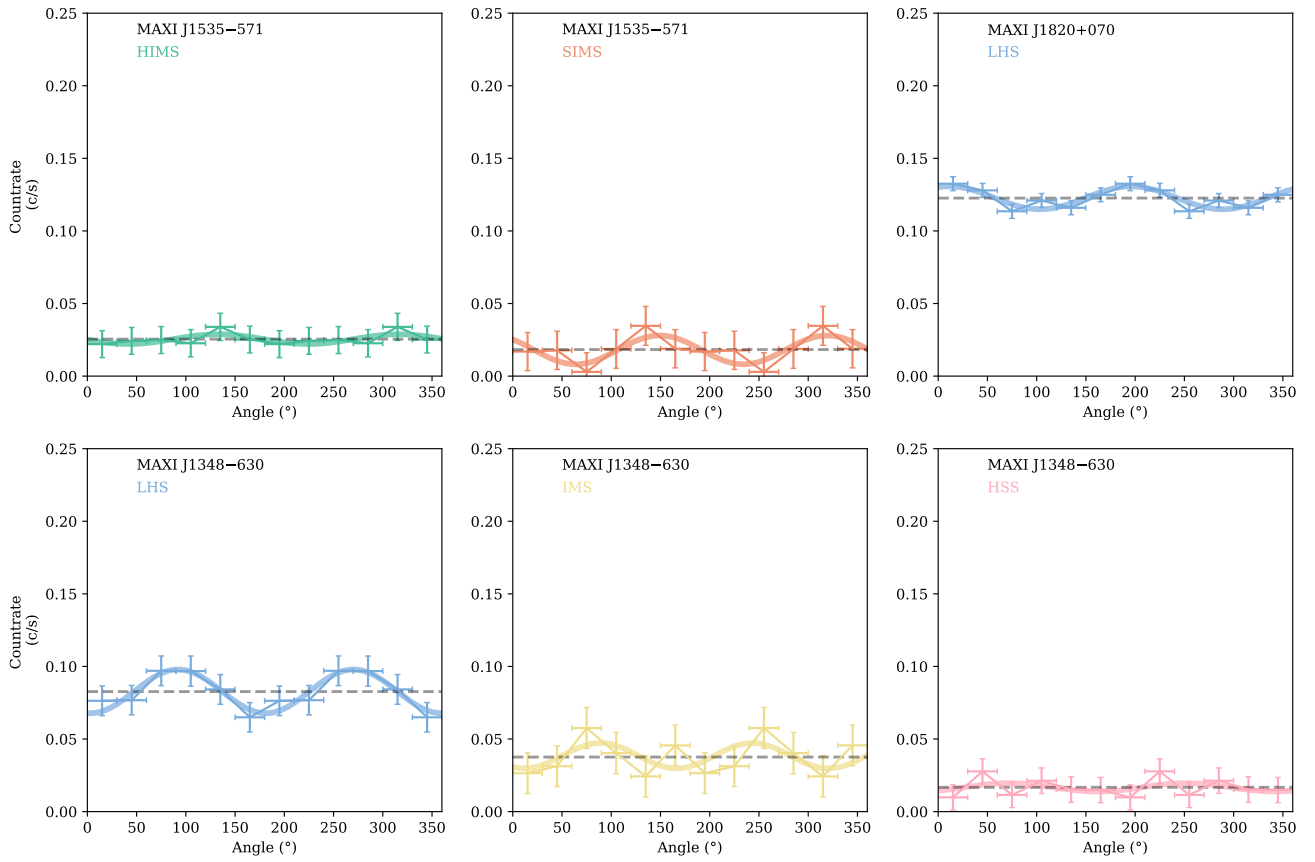


Fig. A.4. Polarigrams of the three sources obtained in the 400–1000 keV energy band range.